On the Synthesis and Adsorption Properties of Single-Unit-Cell Hierarchical Zeolites Made by Rotational Intergrowths

Dandan Xu, Garrett R. Swindlehurst, Haohan Wu, David H. Olson, Xueyi Zhang, and Michael Tsapatsis**

The preparation of hierarchical zeolites usually involves hard or soft templates and multiple synthesis steps, which often prohibit their industrial uses. One way to overcome these issues is to build hierarchical zeolites using repetitive branching, where the intrinsic growth patterns of zeolites, instead of porogenic templates, are utilized. This paper expands on an earlier report to unravel the sequence of events leading to this repetitive branching process for the framework type MFI zeolite structure using small-angle X-ray scattering and transmission electron microscopy. Moreover, adsorption and transport properties of the hierarchical zeolite are probed using 2,2-dimethylbutane, *n*-hexane, and *n*-nonane.

1. Introduction

Hierarchical zeolites are materials with ordered micropores, typical of zeolites (0.5–2 nm), and mesopores that are up to an order of magnitude larger in size (2–50 nm).[1] They can be viewed as a network of zeolitic domains separated by mesopores. This special morphology can give hierarchical zeolites advantages for certain applications in adsorption and catalysis, because the diffusion length in the zeolitic domains becomes smaller and thus diffusion limitations can be eliminated or reduced.[1,2] Moreover, the domains in hierarchical zeolites (such as lamellar and spherical domains) can be isolated and used for other applications including seed layers for thin zeolite membranes for separations.[3–7] One challenge is to prepare hierarchical zeolites with at least one dimension of the domains as small as the size of a zeolite unit cell (e.g., 1 to 5 nm) to eliminate any micropore diffusion resistance and maximize the fraction of external surface area over micropore surface area. At the single-unit-cell limit, the microporous framework is still preserved and, as a result, three-dimensional confinement of adsorbates, reactants and products is still possible as in typical zeolites. However, external surface adsorption is prevalent for bulky molecules that do not fit in the micropores, while configurations with partial confinement, where one part of the molecule resides in the microporous interior and another part resides on the external surface, may be encountered and even dominate catalytic activity and adsorption selectivity.

The preparation of hierarchical zeolites is usually done with two approaches: (1) by the "addition" of framework material, with methods such as crystallization with or without mesopore templates and pillaring,[8–14] and (2) by the "subtraction" of framework material from a zeolite crystal, with methods such as desilication and dealumination.[1,15] However, the preparation of these materials usually requires multiple synthesis steps, and, in many cases, it is challenging to form hierarchical zeolites with ultra-small features of size close to one unit cell. Recently, a new strategy of making hierarchical zeolites with single unit cell domains was discovered.[14] In an environment that encourages the epitaxial intergrowth of two structures with different levels of symmetry, the higher-symmetry structure acts as a connector to connect the lower-symmetry structures to create branching. (**Figure 1**) After this process is repeated, a hierarchical zeolite is formed where the mesopore dimensions are determined by the frequency of branching. Although the work described here features the intergrowth of MFI [a zeolite structure that contains sinusoidal 10-member ring (10-MR) channels along the a axis, interconnected with straight 10-MR channels along the b axis] and MEL (a zeolite structure that contains straight 10-MR channels along the a axis, interconnected with straight 10-MR channels along the b axis) to generate a self-pillared pentasil (SPP) hierarchical zeolite, the approach could be generalized. Intergrowths between other zeolite structures, such as EMT/FAU,[16] ETS-4/ETS-10,[17] CAN/SOD,[18] MFI,[19] and CHA,[20] are common, and could also be used to prepare hierarchical zeolites. Recently, FAU and MFI hierarchical materials have been prepared using this branching approach.[12,13] However, only in the case of MFI as reported in Ref.[14] and here, single unit cell (2 nm) layers are produced, in all other cases, the layers are much thicker.

In this paper, we followed the formation process of self-pillared pentasil zeolite (SPP) by transmission electron

D. Xu, G. R. Swindlehurst, X. Zhang, Prof. M. Tsapatsis
Department of Chemical Engineering
and Materials Science
University of Minnesota, 421 Washington Ave SE,
Minneapolis, MN, 55455, USA
E-mail: zhang914@umn.edu; tsapatsis@umn.edu
Dr. H. Wu
Department of Materials Science and Engineering
Rutgers University
607 Taylor Road, Piscataway, NJ, 08854, USA
Dr. D. H. Olson
Department of Chemistry and Chemical Biology
Rutgers University
610 Taylor Road, Piscataway, NJ, 08854, USA

DOI: 10.1002/adfm.201301975

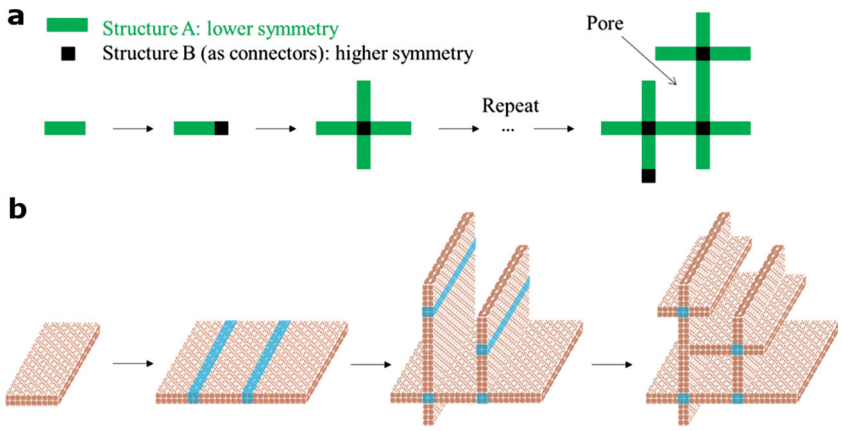

Figure 1. a) When two structures with two different levels of symmetry can intergrow, the higher-symmetry structure may serve as a connector to connect the lower-symmetry structure. If this process is repeated, hierarchical materials can be formed. b) A hierarchical zeolite, self-pillared pentasil (SPP), formed by the intergrowth of MEL and MFI is shown. Here, MFI (red) has the lower symmetry (*Pnma*) and MEL (blue) has the higher symmetry ($I\bar{4}m2$)

microscopy (TEM) and small-angle X-ray scattering (SAXS). Three phases of crystal growth were observed, where amorphous precursor nanoparticles, one-unit-cell MFI nanosheets, and self-pillared particles are formed sequentially. We discuss these findings in the context of previous MFI nucleation and growth models and point to some unique features observed during SPP growth. We also present new results in hydrocarbon adsorption in SPP and compare with conventional MFI.

2. Results and Discussion

2.1. Synthesis

In our earlier report on SPP,[14] the focus was on the use of tetrabutylphosphonium hydroxide (TBPOH) as SDA, however, as mentioned in the supporting information of that report, tetrabutylammonium hydroxide (TBAOH) can also be used to obtain similar orthogonally intergrown 2 nm MFI lamellae. This fact is further elaborated here. **Figure 2** shows self-pillared MFI prepared using TBPOH and TBAOH from various sources. It appears that the synthesis is robust and insensitive to the source of SDA. As seen in **Figure 3**, the argon adsorption/desorption isotherms of SPP made with these two SDAs show both the micropores of MFI and the characteristic mesopores ranging from 2–7 nm. The adsorption isotherms are identical up to $p/p_0 = 0.6$, indicating that the two materials have the same textural properties in the micropore and mesopore regions. Thus, TBPOH and TBAOH can be used interchangeably for the synthesis to yield the characteristic hierarchical porosity of SPP.

Temperature and time are important parameters for the synthesis of SPP. As temperatures in laboratory ovens may vary from nominal indicated temperature, fine-tuning of

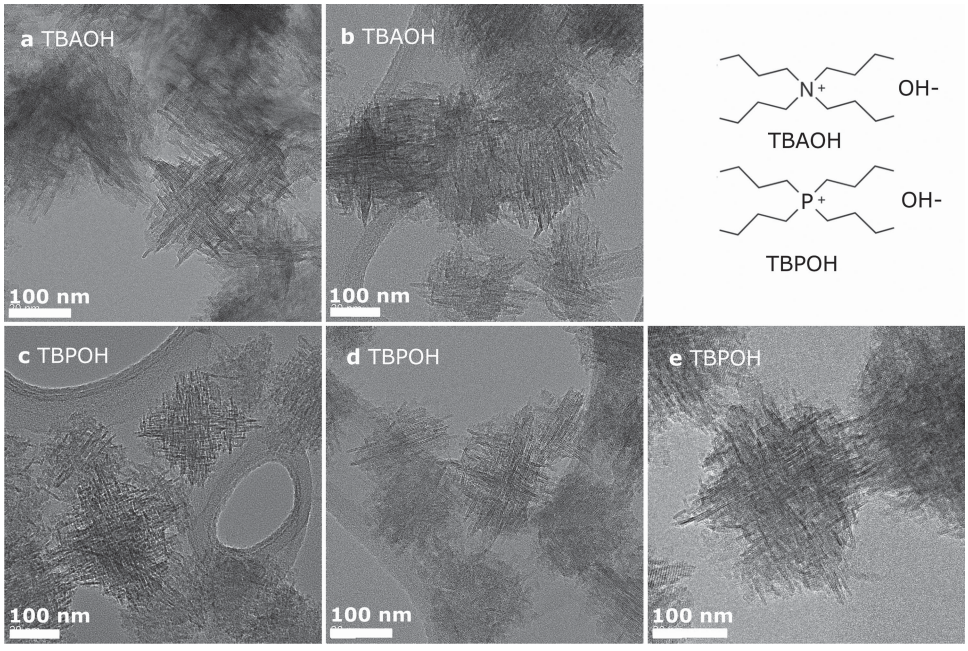

Figure 2. Self-pillared pentasil (SPP) made from tetrabutylammonium hydroxide (TBAOH) and tetrabutylphosphonium hydroxide (TBPOH) as structure-directing agents (SDA). The SDAs are a) TBAOH from SACHEM, b) TBAOH from Sigma-Aldrich, c) TBPOH from SACHEM, d) TBPOH from Sigma-Aldrich, and e) TBPOH from TCI America.

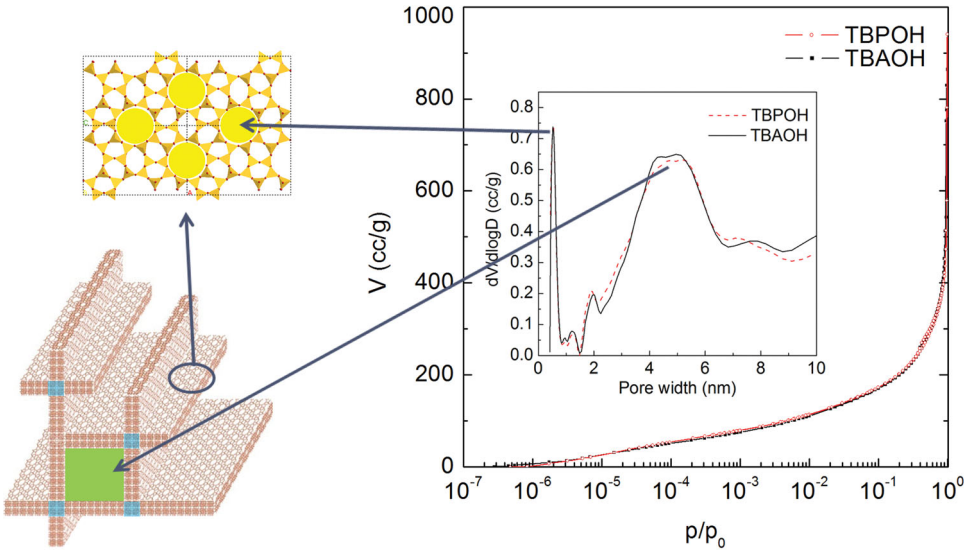

Figure 3. The hierarchical porosity of the self-pillared pentasil (SPP) zeolite as determined from argon adsorption. The pore size distribution (inset, fitted from non-local density functional theory (NLDFT) method) shows that SPP has the typical micropores of MFI (0.52 nm) and characteristic mesopores within the 2–7 nm range. Samples made with TBPOH and TBAOH show similar micro- and mesoporosity.

temperature and time may be required to obtain high-quality SPP samples (i.e., minimize presence of any amorphous materials and limit the growth of the lamellae so they do not become thicker than one unit cell). Based on our previous report,[14] we optimized the synthesis conditions, and found that a hydrothermal synthesis temperature of 120 °C, rather than 115 °C, is preferred for high-quality SPP. In addition to synthesis temperature, the purity of SDA is also crucial for producing SPP morphology. SDAs that successfully give SPP morphology are shown in Figure 2, while impure SDAs (results not shown) compromise SPP sample quality.

In order to understand the sequence of events leading to the formation of the self-pillared pentasil zeolite, one composition (1 SiO_2:0.3 TBPOH:10 H_2O:4 EtOH) was followed over time. A clear sol was obtained after the hydrolysis of tetraethyl orthosilicate (TEOS), indicating the absence of large aggregates. A clear synthesis mixture gives the possibility of studying the system evolution with small-angle X-ray scattering (SAXS), which could identify the size and shape of ultra-small particles, especially when the particles are uniform.[21] This clear system was heated firstly at 80 °C for 48 h, then at 120 °C for up to 40 h. During the hydrothermal synthesis at 120 °C, samples from the synthesis mixtures were collected and analyzed by SAXS and TEM.

The SAXS and TEM experiments revealed three phases of evolution.

During the first phase, with increasing hydrothermal synthesis time from 0–7 h, the SAXS patterns (**Figure 4**) show the existence of a population of globular nanoparticles, which grows slightly in concentration and/or density. The particle size obtained from an IFT (indirect Fourier transform) analysis of the SAXS patterns is 4 nm (Figure 4(b)). No evidence for crystallinity is observed by TEM for samples collected up to 7 h. The existence of amorphous precursor nanoparticles is expected based on earlier studies of MFI precursor sols: for example, the synthesis of TPA-silicalite-1 in a TPAOH (tetrapropylammonium hydroxide)-TEOS-water system involved the formation of small precursor nanoparticles.[21,22] These particles are formed spontaneously upon TEOS hydrolysis and remain nearly constant in size during the initial phases of hydrothermal growth.

After 8.5 h, the growth entered the second phase, where the low-*q* intensity increase indicated the appearance of particles with a larger characteristic dimension. (Figure 4) IFT analysis from these patterns showed that in addition to the 4 nm nanoparticles, another length scale (10–50 nm) emerged. Interestingly, the intensity increase in the low-*q* region is not accompanied by intensity loss in the higher-*q* region. Parallel HRTEM studies confirmed the emergence of a new population of crystalline particles. Consistent with SAXS, the lateral size of these crystalline particles ranged from 10–50 nm. They were found to be highly crystalline MFI. (Figure 4(c),(d)) The low contrast as well as the uniform orientation of the particles suggested that these particles are nanosheets, thin along the b-direction and wide along the a- and c-directions. Previously reported AFM images confirmed that the thickness of these particles is around 2 nm.[14] In the formation of TPA-silicalite-1, a closely related system, Davis et al. and Kumar et al. found that amorphous precursor nanoparticles increased in size, then aggregated to form 100 nm-sized aggregates, which, subsequently, transformed to MFI.[21,22] Examples of intermediate amorphous aggregates also exist in the formation of other zeolites, where at a certain stage amorphous particles transform to crystals by parts.[23] Unlike these previous observations in zeolite systems, where zeolite crystals nucleate within amorphous aggregates, the formation of SPP either does not involve amorphous-to-crystal evolution (i.e., crystals directly form from the clear synthesis sols), or this transformation is much faster than the formation rate of the amorphous aggregates.

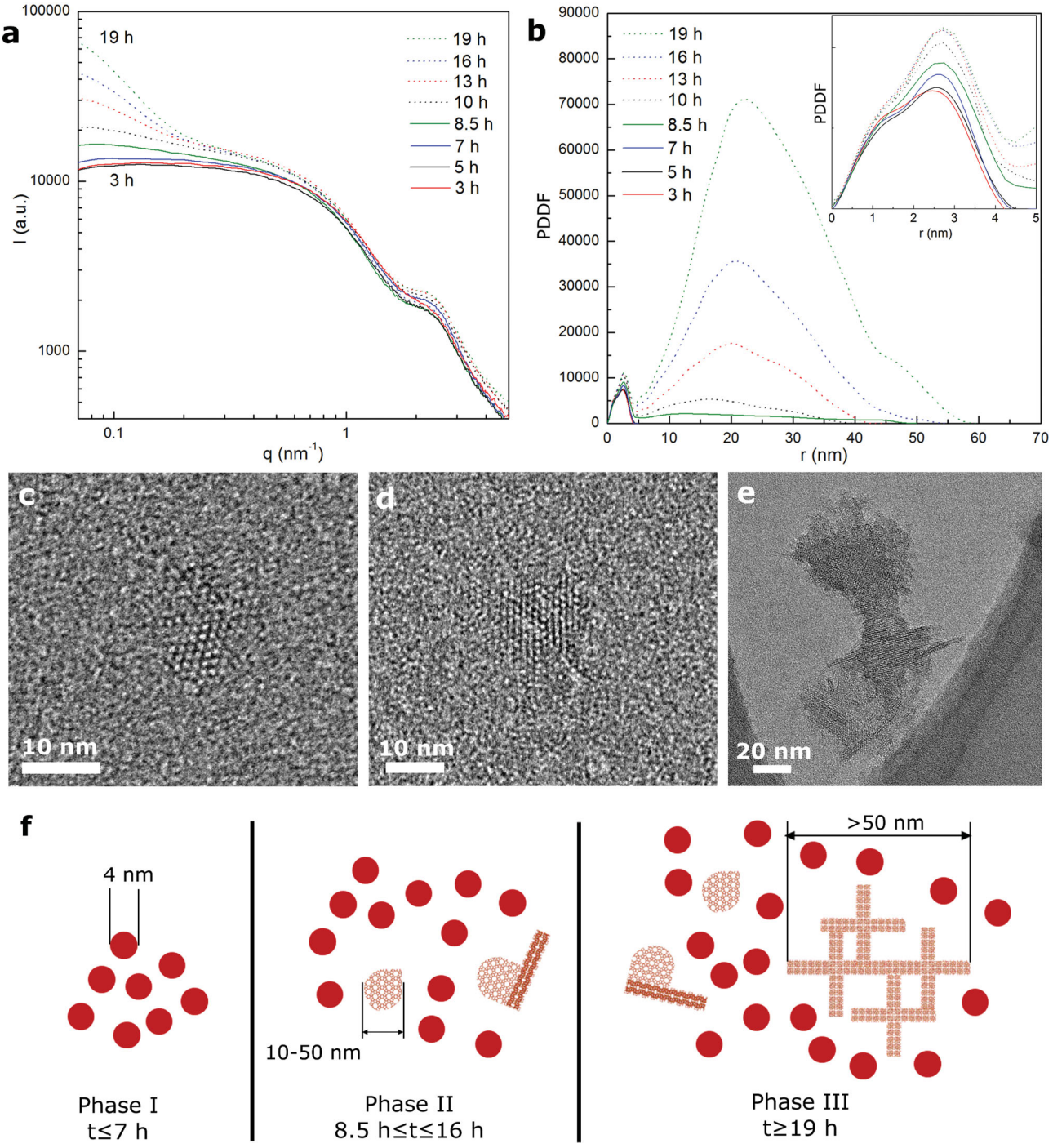

Figure 4. Small-angle X-ray scattering (SAXS) data (a) and corresponding pair distance distribution functions (PDDF) (b) from sols (with composition 1 SiO_2:0.3 SDA:10 H_2O:4 EtOH) heated at 80 °C for 48 h and then at 120 °C for 3, 5, 7, 8.5, 10, 13, 16, and 19 h. Representative transmission electron microscopy (TEM) images from the solids contained in the sols after c) 8.5 h, d) 10 h, and e) 19 h at 120 °C. A schematic of the three phases identified is shown in (f).

To our knowledge, the coexistence of precursor nanoparticles and MFI nanosheets is a unique characteristic of the SPP system. The absence of any amorphous aggregates (detectable by TEM) at this MFI nucleation phase is also a unique feature of this system among reported MFI syntheses.

During the second phase and as early as 8.5 h, crystalline nanoparticles clearly started to exhibit lamellar breakouts on the MFI nanosheets (**Figure 5**). This is the point where the rotational intergrowth starts. TBAOH and TBPOH are structure-directing agents that are known to direct the intergrowth of

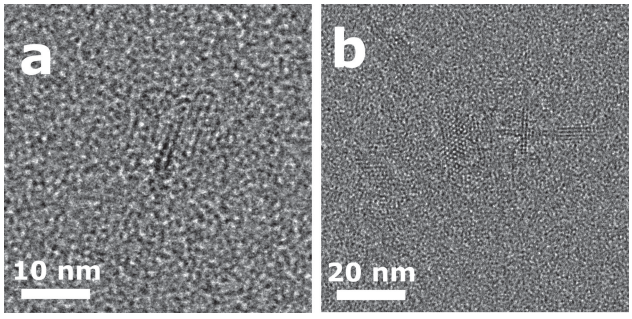

Figure 5. High-resolution transmission electron microscopy (HRTEM) images showing rotational intergrowths observed after 8.5 (a) and 10 (b) h hydrothermal synthesis.

MFI and MEL,[24,25] i.e., both MFI and MEL can coexist in one crystal with fully connected SiO_4 tetrahedra or with the presence of Si-OH defects.[26] In the synthesis of SPP, it seems that these SDAs create an environment that encourages the intergrowth of MFI and MEL. Thus, MEL can be formed onto the MFI nanosheets, and new MFI layers can emerge out of MEL. If the structures of MFI and MEL are compared, one notices that although they have the same building units (the pentasil unit), they differ in symmetry. On MFI nanosheets, MEL can only be incorporated along its a-direction, which could lead to branching in 2 opposite directions; however, on MEL, MFI can be formed along both (equivalent) a- and b- directions, which could lead to branching in 4 directions. When MEL is formed, it can act as connector to connect new features that lead to branching (one-unit-cell nanosheets, in this case). If these newly formed features also contain MEL, another generation of branching could happen. The above-mentioned intergrowth of MFI and MEL is discussed in more detail in our previous report, where the possible structures are enumerated.[14] This repetitive rotational intergrowth led to anisotropic particle shapes, and also wider particle size distributions.

In the third phase, as seen in the SAXS patterns at low-*q* range, much larger particles were observed: the crystalline particles after 19 h hydrothermal synthesis (Figure 4(e)) are much larger comparing to the particles after 10 h synthesis (Figure 4(d)). Finally, with complete hydrothermal synthesis after 40 h, the crystals are fully developed with the typical self-pillared morphology (Figure 2) and their long dimensions are beyond the low angle resolution limit of SAXS.

The presence of MFI nanosheets at early phases of growth taken together with the presence of orthogonally arranged lamellae in SPP particles after 40 h heating suggested that these nanosheets are responsible for the formation of the lamellae, since they have the same thickness and crystallographic orientation. Two possible mechanisms exist for the formation of the intergrown crystals: oriented aggregation, and direct growth of nanosheets by addition of silicate species. Oriented aggregation is a non-classical crystal growth mechanism, according to which crystalline particles aggregate in a crystallographically aligned manner.[21,22,27,28] If oriented aggregation of the nanosheets was the formation mechanisms of SPP, one would expect that the SPP particles would have a more open structure. Instead of the 2–7 nm mesopores, the mesopore dimensions would have been similar to the dimension of the nanosheets, i.e., 10–50 nm. Therefore, direct growth by addition of molecular silicate species or by aggregation with precursor nanoparticles seems to be more likely mechanisms for the formation of SPP.

2.2. Adsorption

In our previous report,[14] reaction rates over Al-containing SPP were compared with those over conventional MFI and it was demonstrated that intracrystalline diffusion limitations for certain reactions can be eliminated. Here, we compare adsorption of 2,2-dimethylbutane (2,2-DMB) in SPP and a conventional ZSM-5 (H-ZSM-5(36)). At 90 °C, 2,2-DMB adsorption in H-ZSM-5(36) took place slowly to reach 59 mg g^{-1} after 10 h, close to the expected value of 60 mg g^{-1} corresponding to 1 molecule per intersection. (**Figure 6**(a)) A similar level of adsorption (55 mg g^{-1}) was reached very fast in the case of SPP. With conventional MFI as a reference, the amount adsorbed on SPP (92% of the amount adsorbed at equilibrium on H-ZSM-5(36)) can be interpreted as an indication of "crystallinity" or microporosity of the SPP sample. The SPP adsorption rate was too fast to be reliably measured with the equipment used at 90 °C. At 30 °C (Figure 6(b)), 2,2-DMB approached 60 mg g^{-1} after 1000 min while SPP adsorbed 100 mg g^{-1} at a very fast but measurable rate. From the uptake curves, (D/r^2) values at 30 °C were determined to be 2.6×10^{-5} and 4.2×10^{-3} s^{-1} for the conventional and SPP zeolites, respectively. These values of (D/r^2) suggest that the conventional and SPP zeolites have a characteristic diffusion length ratio of approximately 13. If we estimate the diffusivity of 2,2-DMB using the reported value of 3×10^{-18} m^2 s^{-1} at 400 K (127 °C) and activation energy of 66 kJ mol^{-1},[29] we obtain $D_{2,2\text{-DMB}}(30\ °C) = 5 \times 10^{-21}$ m^2 s^{-1}, which for 1 nm diffusion length gives a (D/r^2) value in remarkable agreement with the one determined experimentally for SPP. Given (i) the uncertainty in diffusivity measurements and extrapolations, (ii) the possible contribution of mesopore and pore mouth resistances, and (iii) the questionable applicability of a continuum model to describe transport at the single-unit-cell level, this remarkable agreement should not be over-interpreted. However, it strongly suggests the attainment of nm-scale characteristic diffusion lengths for 2,2-DMB in SPP. The results also indicate that at 90 °C SPP exhibits 2,2-DMB micropore adsorption comparable to the conventional zeolite (Figure 6(a)). At a lower temperature (Figure 6(b)), significant adsorption in the mesopores of SPP also occurs, which resulted in much larger total amount adsorbed than that expected on micropores alone.

Although 2,2-DMB adsorption rates and equilibrium adsorption under the conditions investigated (115 torr at 30 °C and 90 °C) can be qualitatively explained by considering the differences of porosity between a conventional zeolite (H-ZSM-5(36)) and the hierarchical SPP, the case for the longer *n*-hexane (~0.8 nm) and *n*-nonane (~1.2 nm) adsorption is more complicated, possibly due to "edge effects", i.e., adsorption with only a part of the molecule being confined in the microporous interior and the remaining part located outside of the micropores.

For *n*-hexane (**Figure 7**), adsorption in SPP was consistently lower than that obtained in H-ZSM-5(36) over the entire range of *n*-hexane pressures and adsorption temperatures investigated

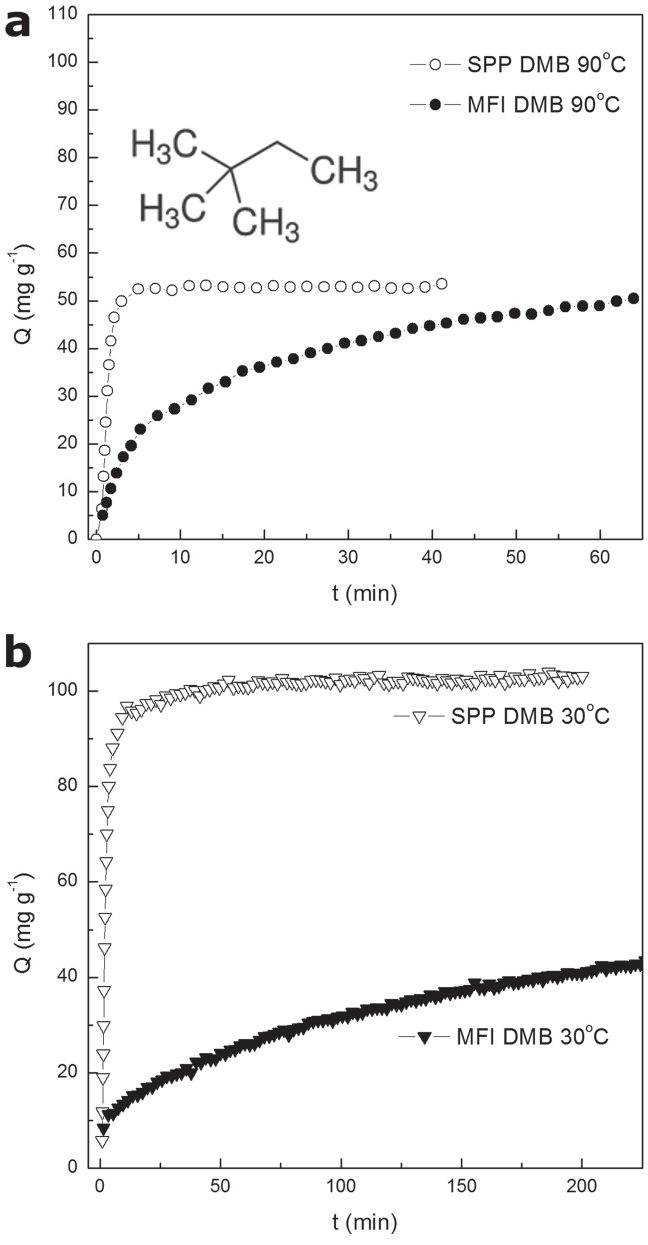

Figure 6. Adsorption of 2,2-dimethylbutane (2,2-DMB) in conventional MFI and pure silica self-pillared pentasil (SPP) at a) 90 °C and b) 30 °C (2,2-DMB pressure is 115 torr).

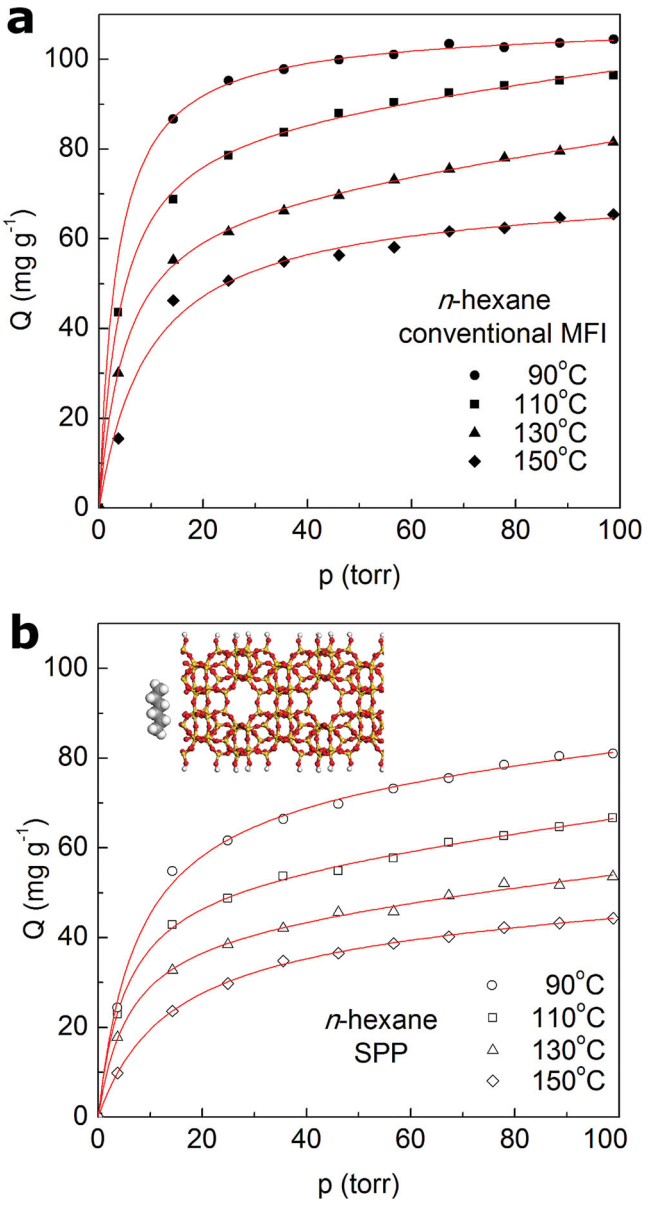

Figure 7. Adsorption isotherms of *n*-hexane in conventional MFI (a) and pure silica self-pillared pentasil (SPP) (b) at 90 °C, 110 °C, 130 °C, and 150 °C. The data (open and closed symbols) are given and also fitted with $Q = K_1 p + \frac{K_2 K_3 p}{1+K_3 p}$ (solid lines).

indicating that the SPP mesopores do not contribute enough adsorption to compensate for the reduced adsorption due to loss of microporosity. For *n*-nonane (**Figure 8**), the situation was similar except for the lowest temperatures tested (90 and 110 °C), where at the highest pressure range (above 0.5 and 1.5 torr for 90 °C and 110 °C, respectively) SPP adsorption matched and even exceeded adsorption in the conventional zeolite. At certain conditions, the differences are striking. For example, at 150 °C the adsorbed amount at 1.2 torr in ZSM-5(36) was 78 mg g^{-1}, while in SPP was only 40 mg g^{-1}. The substantially lowered adsorption at higher temperatures can be ascribed to "edge effects" mentioned above. Consistent with this scenario of partial confinement, preliminary estimations of the isosteric heat of adsorption (extracted from Henry's constants determined in the range of 150–230 °C) indicate lower values for SPP by ~10 kJ mol^{-1} (61 vs. 51 kJ mol^{-1}) and ~25 kJ mol^{-1} (95 vs. 70 kJ mol^{-1}) with *n*-hexane and *n*-nonane as adsorbates, respectively. These findings require further examination and validation as this reduced interaction, together with the short micropore diffusion path length, will influence the catalytic performance of these new materials. It would also be interesting to see if molecular simulations can capture this adsorption behavior and provide a molecular level understanding.

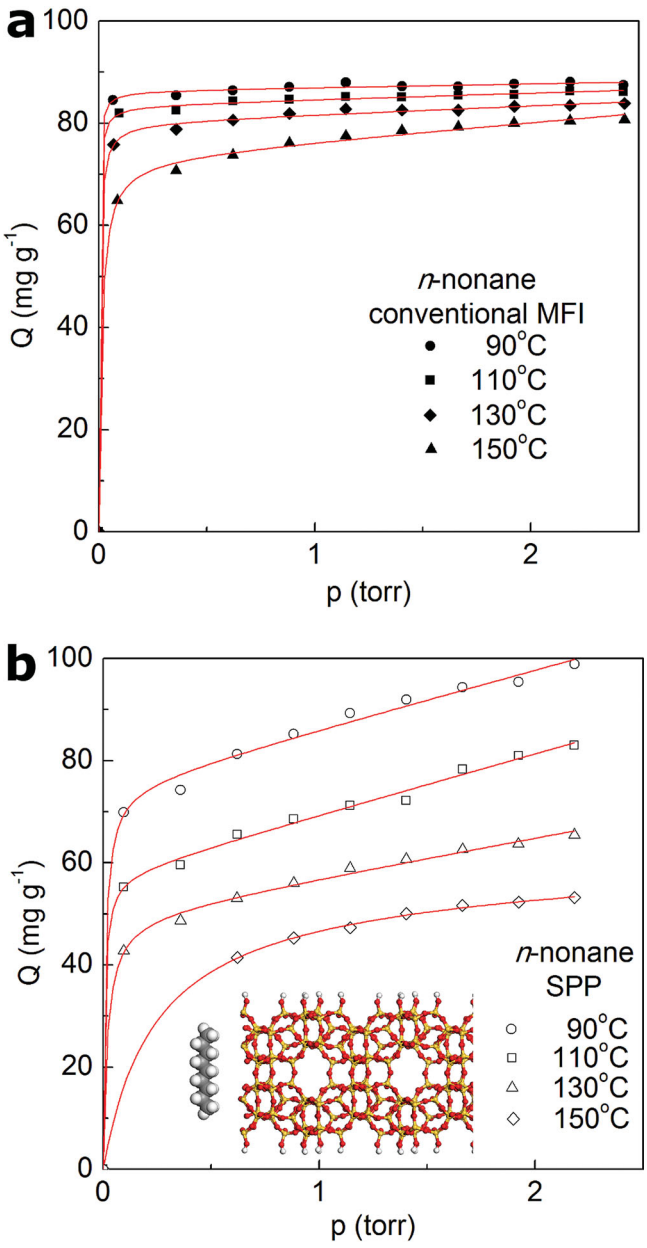

Figure 8. Adsorption isotherms of *n*-nonane in conventional MFI (a) and pure silica self-pillared pentasil (SPP) (b) at 90 °C, 110 °C, 130 °C, and 150 °C. The data (open and closed symbols) are given and also fitted with $Q = K_1 p + \frac{K_2 K_3 p}{1+K_3 p}$ (solid lines).

3. Conclusions

Hierarchical zeolites can be formed by repetitive rotational intergrowth of two structures. Self-pillared pentasil zeolite is one example of a hierarchical zeolite composed of intergrown 2 nm MFI lamellae, formed by one step hydrothermal synthesis. In this paper, the growth process of SPP was followed over time using TEM and SAXS to reveal three phases of crystal growth. The adsorption properties of this hierarchical zeolite were explored using hydrocarbons, and showed distinct behavior compared to conventional MFI.

4. Experimental Section

Zeolite Synthesis: The silica sols for SPP synthesis were prepared with the composition 1 SiO_2:0.3 SDA:10 H_2O:4 EtOH, where SDA (structure-directing agent) was either tetrabutylphosphonium hydroxide (TBPOH, 40% by weight, Sigma-Aldrich, TCI America or SACHEM) or tetrabutylammonium hydroxide (TBAOH, 40% by weight, Sigma-Aldrich or SACHEM). The SDA solution was firstly added dropwise into tetraethylorthosilicate (TEOS, 98%, Sigma-Aldrich) with vigorous stirring until the system turns clear. Then distilled water was added into the clear system at room temperature. The clear sol was sealed with Teflon tape and aged at 80 °C in a Teflon bottle with continuous stirring. After 48 h aging, the clear sol was quickly transferred to a Teflon-lined stainless steel autoclave, sealed and heated for 3–40 h in a pre-heated oven at 120 °C. The final sols after heating were then collected for further characterizations. Conventional MFI was prepared following Ref. [30].

Characterization: SAXSess (Anton-Parr) was used to obtain small-angle X-ray scattering patterns from the sols after hydrothermal treatment. The sols were placed into vacuum-tight 1 mm quartz capillary. All measurements were carried out at room temperature (25 °C). The scattering vector q was calculated from the scattering angle 2θ through $q = 4\pi\lambda^{-1}\sin\theta$. Scattering from an equivalent water-ethanol mixture was used as a background pattern and subtracted from all sample scattering patterns. Patterns were then de-smeared from the beam profile and fitted using the GIFT program.[31] Pair distance distribution functions (PDDF) were obtained by indirect Fourier transform of the fitted data.

The synthesis sols obtained at different time were diluted 10 times (1:10 by volume) with distilled water, and used for TEM samples. TEM specimens were prepared by placing droplets of the diluted sol onto the copper grid coated with ultra-thin carbon film and holey carbon film (Ted Pella Inc.). The non-diluted TEM specimen was prepared by drawing a thin line onto the same type of grid from the clear sols without any dilution, and then spreading over the copper grid. All images included here, except Figure 5(b), are from diluted sols. Comparative experiments, not shown here, using diluted and non-diluted samples indicate that the morphology of the MFI particles is not altered by the dilution. The specimens were dried at room temperature. TEM imaging was performed on an FEI Tecnai G^2 F30 TEM operating at 300 kV. All TEM images were captured using a CCD camera.

Argon (87.3 K) adsorption was performed using a commercially available automatic manometric sorption analyzer (Quantachrome Instruments Autosorb iQ MP). Prior to adsorption measurements, the samples were outgassed at 300 °C for 16 h under turbomolecular pump vacuum. Full micro- and mesopore size distributions were calculated from the argon isotherms using the argon on zeolites/silica cylindrical pore adsorption branch method.[32]

Hydrocarbon Adsorption: Adsorption measurements were made using a computer controlled thermogravimetric balance consisting of a TA51 electrobalance and associated TA-2000/PC control system. This one atmosphere, gas flow through electrobalance system was controlled via Macintosh-based LabView control software, Kinetic Systems interface, mass flow controllers and Eurotherm temperature controller. Hydrocarbon pressures for the isotherms were obtained by blending a pure nitrogen gas stream with a nitrogen gas saturated with the hydrocarbon at 18 °C.

Acknowledgements

The authors acknowledge support from the Catalysis Center for Energy Innovation (award DESC00001004), an Energy Frontier Research Center funded by the U.S. Department of Energy, Office of Science, Office of Basic Energy Sciences. Portions of this work were conducted at the University of Minnesota Characterization Facility, which receives partial support from NSF through the NNIN program. DHO and HW are pleased to acknowledge the general encouragement of Professor Jing Li and her group members for their assistance.

Received: June 9, 2013
Revised: July 15, 2013
Published online: September 23, 2013

[1] J. Perez-Ramirez, C. H. Christensen, K. Egeblad, C. H. Christensen, J. C. Groen, *Chem. Soc. Rev.* **2008**, *37*, 2530–2542.
[2] D. Liu, A. Bhan, M. Tsapatsis, S. Al Hashimi, *ACS Catal.* **2011**, *1*, 7–17.
[3] A. Corma, V. Fornes, S. B. Pergher, T. L. M. Maesen, J. G. Buglass, *Nature* **1998**, *396*, 353–356.
[4] Y. X. Wang, H. Gies, B. Marler, U. Muller, *Chem. Mater.* **2005**, *17*, 43–49.
[5] M. Choi, K. Na, J. Kim, Y. Sakamoto, O. Terasaki, R. Ryoo, *Nature* **2009**, *461*, 246–249.
[6] W. J. Roth, D. L. Dorset, *Microporous Mesoporous Mater.* **2011**, *142*, 32–36.
[7] P.-S. Lee, X. Zhang, J. A. Stoeger, A. Malek, W. Fan, S. Kumar, W. C. Yoo, S. Al Hashimi, R. L. Penn, A. Stein, M. Tsapatsis, *J. Am. Chem. Soc.* **2011**, *133*, 493–502.
[8] J. Wang, W. Yue, W. Zhou, M.-O. Coppens, *Microporous Mesoporous Mater.* **2009**, *120*, 19–28.
[9] D. P. Serrano, J. Aguado, J. M. Escola, A. Peral, G. Morales, E. Abella, *Catal. Today* **2011**, *168*, 86–95.
[10] K. Na, C. Jo, J. Kim, K. Cho, J. Jung, Y. Seo, R. J. Messinger, B. F. Chmelka, R. Ryoo, *Science* **2011**, *333*, 328–332.
[11] W. J. Roth, C. T. Kresge, J. C. Vartuli, M. E. Leonowicz, A. S. Fung, S. B. McCullen, in *Studies in Surface Science and Catalysis*, Vol. *94* (Eds: H. K. Beyer, H. G. Karge, I. Kiricsi, J. B. Nagy), Elsevier, Amsterdam **1995**, pp.301–308.
[12] W. Chaikittisilp, Y. Suzuki, R. R. Mukti, T. Suzuki, K. Sugita, K. Itabashi, A. Shimojima, T. Okubo, *Angew. Chem.* **2013**, *52*, 3355–3359.
[13] A. Inayat, I. Knoke, E. Spiecker, W. Schwieger, *Angew. Chem.* **2012**, *51*, 3.
[14] X. Zhang, D. Liu, D. Xu, S. Asahina, K. A. Cychosz, K. V. Agrawal, Y. Al Wahedi, A. Bhan, S. Al Hashimi, O. Terasaki, M. Thommes, M. Tsapatsis, *Science* **2012**, *336*, 1684–1687.
[15] M. Ogura, S. Y. Shinomiya, J. Tateno, Y. Nara, M. Nomura, E. Kikuchi, M. Matsukata, *Appl. Catal. A* **2001**, *219*, 33–43.
[16] M. M. J. Treacy, D. E. W. Vaughan, K. G. Strohmaier, J. M. Newsam, *Proc. R. Soc. A* **1996**, *452*, 813–840.
[17] H. K. Jeong, J. Krohn, K. Sujaoti, M. Tsapatsis, *J. Am. Chem. Soc.* **2002**, *124*, 12966–12968.
[18] T. Okubo, T. Wakihara, J. Plevert, S. Nair, M. Tsapatsis, Y. Ogawa, H. Komiyama, M. Yoshimura, M. Davis, *Angew. Chem.* **2001**, *40*, 1069–1071.
[19] L. Karwacki, M. H. F. Kox, D. A. M. de Winter, M. R. Drury, J. D. Meeldijk, E. Stavitski, W. Schmidt, M. Mertens, P. Cubillas, N. John, A. Chan, N. Kahn, S. R. Bare, M. Anderson, J. Kornatowski, B. M. Weckhuysen, *Nat. Mater.* **2009**, *8*, 959–965.
[20] G. R. Millward, S. Ramdas, J. M. Thomas, *Proc. R. Soc. A* **1985**, *399*, 57–71.
[21] T. M. Davis, T. O. Drews, H. Ramanan, C. He, J. S. Dong, H. Schnablegger, M. A. Katsoulakis, E. Kokkoli, A. V. McCormick, R. L. Penn, M. Tsapatsis, *Nat. Mater.* **2006**, *5*, 400–408.
[22] S. Kumar, Z. Wang, R. L. Penn, M. Tsapatsis, *J. Am. Chem. Soc.* **2008**, *130*, 17284–17288.
[23] S. Mintova, N. H. Olson, V. Valtchev, T. Bein, *Science* **1999**, *283*, 958–960.
[24] Z. J. Li, C. M. Lew, S. Li, D. I. Medina, Y. S. Yan, *J. Phys. Chem. B* **2005**, *109*, 8652–8658.
[25] L. Y. Hou, L. B. Sand, in *Proceeding of the Sixth International Zeolite Conference: Reno, USA, 10–15 July 1983* (Eds: D. Olson, A. Bisio), Butterworths Ltd., Canda **1984**, pp.887–893.
[26] T. Ohsuna, O. Terasaki, Y. Nakagawa, S. I. Zones, K. Hiraga, *J. Phys. Chem. B* **1997**, *101*, 9881–9885.
[27] V. M. Yuwono, N. D. Burrows, J. A. Soltis, R. L. Penn, *J. Am. Chem. Soc.* **2010**, *132*, 2163–2165.
[28] D. Liang, L. R. A. Follens, A. Aerts, J. A. Martens, G. Van Tendeloo, C. E. A. Kirschhock, *J. Phys. Chem. C* **2007**, *111*, 14283–14285.
[29] J. Karger, Douglas M. Ruthven, D. N. Theodorou, *Diffusion in Nanoporous Materials*, Vol. *2*, Wiley-VCH, Germany **2012**, p.667.
[30] Robert J. Argauer, George R. Landolt, *US Patent 3*, 702, 886, **1972**.
[31] A. Bergmann, G. Fritz, O. Glatter, *J. Appl. Crystallogr.* **2000**, *33*, 1212–1216.
[32] P. I. Ravikovitch, A. V. Neimark, *Colloids Surf., A* **2001**, *187*, 11–21.